Science Advances

AAAS

advances.sciencemag.org/cgi/content/full/1/10/e1500854/DC1

Supplementary Materials for

Coherent driving and freezing of bosonic matter wave in an optical Lieb lattice

Shintaro Taie, Hideki Ozawa, Tomohiro Ichinose, Takuei Nishio, Shuta Nakajima, Yoshiro Takahashi

Published 20 November 2015, *Sci. Adv.* **1**, e1500854 (2015)
DOI: 10.1126/sciadv.1500854

The PDF file includes:

Supplementary Materials

S1. Calibration of the relative phase

Upper images in **Fig. S1 (A)** shows time-of-flight absorption images of a ^{174}Yb BEC loaded into an optical lattice at the phase $\psi = \pi/2$ and $\psi = 0$, leading to lattice potential landscapes shown in the lower images. In the case of $\psi = \pi/2$, the ground state wave function distributes over all three sites in a unit cell. On the other hand, for $\psi = 0$ atoms are concentrated on a square lattice composed of *A*-sites. This feature is reflected in a momentum distribution of a BEC, where the fraction of zero momentum coherent peak becomes much larger for $\psi = \pi/2$ due to the large tunneling amplitude. In the case of $\psi = 0$, strong confinement to the *A*-sites makes 1st order peaks comparable to the central peak. In addition, small tunneling ($J/k_B \sim 0.1$nK) causes the emergence of visible thermal component.

The phase dependence of the each momentum peak of a BEC is shown in **Fig. S1 (B)**. The experimental data are well reproduced by the non-interacting band calculation, which is utilized for the calibration of ψ.

S2. Tight-binding model for the optical Lieb lattice

Here we present the derivation of the tight-binding model describing our optical Lieb lattice. The kinetic energy part of the tight-binding Hamiltonian considered here is written in the form

$$\hat{H}_{\mathrm{TB}} = \hat{H}_{\mathrm{Lieb}} + \hat{H}_{\mathrm{BC}} + \hat{H}_{\mathrm{S}} \qquad (1)$$

Here $\hat{H}_{\mathrm{Lieb}}$ represents the part involving nearest-neighbor hopping, $\hat{H}_{\mathrm{BC}}$ next-nearest-neighbor hopping between the *B* and *C* sites, and $\hat{H}_{\mathrm{S}}$ the Hamiltonian within each sublattice. These terms are explicitly expressed in the second quantized form as

$$\begin{aligned}
\hat{H}_{\mathrm{Lieb}} &= -J\sum_{k,l}\left[\left(\hat{a}^{\dagger}_{(k,l),A}\hat{a}_{(k,l),B} + \hat{a}^{\dagger}_{(k,l),A}\hat{a}_{(k-1,l),B}\right) + \left(\hat{a}^{\dagger}_{(k,l),A}\hat{a}_{(k,l),C} + \hat{a}^{\dagger}_{(k,l),A}\hat{a}_{(k,l-1),C}\right)\right] + \mathrm{H.c.},\\
\hat{H}_{\mathrm{BC}} &= -J_{BC}\sum_{k,l}\left[\left(\hat{a}^{\dagger}_{(k,l),B}\hat{a}_{(k+1,l),C} + \hat{a}^{\dagger}_{(k,l),B}\hat{a}_{(k,l-1),C}\right)\right] + \mathrm{H.c.},\\
\hat{H}_{\mathrm{S}} &= \sum_{k,l}\left[-\sum_{S=A,B}J_{SS}\left(\hat{a}^{\dagger}_{(k,l),S}\hat{a}_{(k+1,l),S} + \mathrm{H.c.}\right) - \sum_{S=A,C}J_{SS}\left(\hat{a}^{\dagger}_{(k,l),S}\hat{a}_{(k,l+1),S} + \mathrm{H.c.}\right) + \sum_{S=A,B,C}E_S\hat{a}^{\dagger}_{(k,l),S}\hat{a}_{(k,l),S}\right],
\end{aligned} \qquad (2)$$

where $\hat{a}_{(k,l),S}$ is the annihilation operator on a site *S* (= *A*, *B*, *C*) in a unit cell labeled by its coordinates $(x, z) = (kd, ld)$. Inclusion of beyond-nearest-neighbor hopping J_{BC} and J_{SS} is necessary to reproduce the band dispersions obtained by the first principle band calculations, especially for shallow lattices. **Figure S2 (A)** shows a sketch of each hopping term. Regarding J_{BC}, we consider terms along the direction $\hat{\mathbf{x}} + \hat{\mathbf{z}}$ only, because our diagonal lattice suppresses the hopping along the $\hat{\mathbf{x}} - \hat{\mathbf{z}}$ direction (see **Fig. S1 (A)**). Similarly, hopping J_{BB} (J_{CC}) is restricted to the *x*- (*z*-)

direction, respectively. In the momentum space representation $\hat{a}_{i,S} = 1/\sqrt{N}\sum_{\mathbf{k}} e^{i\mathbf{k}\cdot\mathbf{x}_{i,S}}\hat{a}_{\mathbf{k},S}$, the Hamiltonian is diagonalized with respect to the momentum indices as

$$\hat{H}_{\mathrm{TB}} = \sum_{\mathbf{k}} \begin{pmatrix} \hat{a}^{\dagger}_{\mathbf{k},A} & \hat{a}^{\dagger}_{\mathbf{k},B} & \hat{a}^{\dagger}_{\mathbf{k},C} \end{pmatrix} T \begin{pmatrix} \hat{a}_{\mathbf{k},A} \\ \hat{a}_{\mathbf{k},B} \\ \hat{a}_{\mathbf{k},C} \end{pmatrix}, \qquad (3)$$

$$T = T_{\mathrm{Lieb}} + T_{\mathrm{BC}} + T_{\mathrm{S}}.$$

Here T is the 3×3 matrix which couples each sublattice, given by

$$T_{\mathrm{Lieb}} = \begin{pmatrix} 0 & -2J\cos(k_x d/2) & -2J\cos(k_z d/2) \\ -2J\cos(k_x d/2) & 0 & 0 \\ -2J\cos(k_z d/2) & 0 & 0 \end{pmatrix},$$

$$T_{\mathrm{BC}} = \begin{pmatrix} 0 & 0 & 0 \\ 0 & 0 & -2J_{BC}\cos(k_x d/2 + k_z d/2) \\ 0 & -2J_{BC}\cos(k_x d/2 + k_z d/2) & 0 \end{pmatrix}, \qquad (4)$$

$$T_{\mathrm{S}} = \begin{pmatrix} E_A - 2J_{AA}[\cos(k_x d) + \cos(k_z d)] & 0 & 0 \\ 0 & E_B - 2J_{BB}\cos(k_x d) & 0 \\ 0 & 0 & E_C - 2J_{CC}\cos(k_z d) \end{pmatrix}.$$

Leaving only T_{Lieb}, we have analytic expressions for the eigenvalues of the Lieb lattce with hopping to the nearest neighbors only, as

$$E_{\pm} = \pm 2J\sqrt{\cos^2(k_x d/2) + \cos^2(k_z d/2)}, \qquad (5)$$
$$E_0 = 0,$$

and the corresponding eigenfunctions

$$|\mathbf{k}, 1\mathrm{st}\rangle = \frac{1}{\sqrt{2}}\left(|\mathbf{k}, A\rangle + \sin\theta_{\mathbf{k}}|\mathbf{k}, B\rangle + \cos\theta_{\mathbf{k}}|\mathbf{k}, C\rangle\right),$$
$$|\mathbf{k}, 2\mathrm{nd}\rangle = \cos\theta_{\mathbf{k}}|\mathbf{k}, B\rangle - \sin\theta_{\mathbf{k}}|\mathbf{k}, C\rangle, \qquad (6)$$
$$|\mathbf{k}, 3\mathrm{rd}\rangle = \frac{1}{\sqrt{2}}\left(|\mathbf{k}, A\rangle - \sin\theta_{\mathbf{k}}|\mathbf{k}, B\rangle - \cos\theta_{\mathbf{k}}|\mathbf{k}, C\rangle\right),$$

with $\tan\theta_{\mathbf{k}} = \cos(k_x d/2)/\cos(k_z d/2)$. To obtain experimentally relevant tight-binding parameters, we perform least-square fitting of the band dispersion obtained by diagonalizing T to the lowest three bands of the first principle calculations. This procedure gives the optimal hopping amplitudes which reproduce the actual band structures, as shown in **Figs. S2 (B)** and **S2 (C)**. Dominant contribution other than the nearest neighbor hopping J comes from J_{BC} and J_{AA}. While the latter does not affect the flat band, J_{BC} eliminates the dark states and causes finite dispersion of the flat band. The ratio J_{BC}/J can be made smaller by increasing lattice depth, or adding another diagonal lattice along the $\hat{\mathbf{x}} + \hat{\mathbf{z}}$ direction.

To derive parameters such as on-site interactions, the above procedure is not sufficient and we need to construct Wannier functions. This involves ambiguity in the definition of the phase of each Bloch state, and we should choose the phase such that resulting Wannier functions are well

localized and minimize non-Hubbard type interactions. Let ($u_{\mathbf{k},A}^{(n)}$, $u_{\mathbf{k},B}^{(n)}$, $u_{\mathbf{k},C}^{(n)}$) (n = 1, 2, 3) to be the eigenvectors of T with the n-th energy band. The Bloch states obtained from the band calculations $|\mathbf{k},n\rangle$ will be written as superposition of the sublattice momentum eigenstates $|\mathbf{k},S\rangle = \hat{a}_{\mathbf{k},S}^{\dagger}|0\rangle$, in the form

$$e^{i\theta(\mathbf{k},n)}|\mathbf{k},n\rangle = \sum_{S=A,B,C} u_{\mathbf{k},S}^{(n)}|\mathbf{k},S\rangle . \qquad (7)$$

Here $\theta(\mathbf{k}, \mathrm{n})$ is unknown phase mentioned above. We follow the procedure similar to that described in (*38*) and choose the phase θ so that all Bloch states constructively interfere at the specific lattice site to give the localized Wannier function on that site:

$$\theta(\mathbf{k},n) = \arg\left[e^{-i\mathbf{k}\cdot\mathbf{x}_{i,S_{\mathrm{Ref}}}} u_{\mathbf{k},S_{\mathrm{Ref}}}^{(n)} \psi_{\mathbf{k}}^{(n)}(x_{i,S_{\mathrm{Ref}}})\right] \qquad (8)$$

where $\psi_{\mathbf{k}}^{(n)}(\mathbf{x})$ is the Bloch wave function $\langle \mathbf{x}|\mathbf{k},n\rangle$. According to Bloch's theorem, the above expression actually does not depend on the choice of unit cell $i = (k, l)$. For each $\mathbf{k}$ and n, we choose appropriate reference sublattice S_{Ref} where the Bloch state has the largest amplitude. After all, the Wanner functions $w_{i,S}(\mathbf{x})$ can be obtained from the Bloch states as

$$w_{i,S}(\mathbf{x}) = \sum_{\mathbf{k}} e^{i\mathbf{k}\cdot\mathbf{x}_{i,S}} \sum_{n=1}^{3} u_{\mathbf{k},S}^{(n)} e^{-i\theta(\mathbf{k},n)} \psi_{\mathbf{k}}^{(n)}(\mathbf{x}) . \qquad (9)$$

Figure S3 (A) shows the calculated Wannier functions of the optical Lieb lattice derived by the above procedure. It can be seen that the three Wannier functions $w_{0,A}$, $w_{0,B}$ and $w_{0,C}$ are well localized at the site *A*, *B* and *C* of the unit cell i = (0, 0), respectively. It should be noted that, due to the difference in the confinement of potential wells, density at the (*BC*)-sublattice becomes higher than that of the *A*-sublattice. On-site interactions in the Hubbard model are proportional to the two-dimensional average density $n = \int dx\,dz \left|w_{i,S}(\mathbf{x})\right|^4$ of the Wannier functions. As shown in **Fig. S3 (B)**, the sublattice dependence of n amounts to ~20% for our lattice.

S3. Momentum distributions in coherent band transfer

In the main paper, coherent transfer of a ground state BEC into the 2nd band of the Lieb lattice is analyzed with the quasimomentum distributions. Here, we show a bare momentum distribution in the transfer process, measured by direct time-of-flight experiment. As mentioned in the main paper, quasimomentum analysis cannot distinguish a condensate in the center of the 2nd band from that in the 3rd band. In contrast, these two states have quite different distributions in the momentum space, as shown in **Fig. S4 (A)**. The 2nd band is characterized by the prominent peaks at $\mathbf{k}$ = ($\pm 2k_{\mathrm{L}}$, 0) and (0, $\pm 2k_{\mathrm{L}}$), and vanishing central peak due to the destructive interference of the wave function on the *B*- and *C*-sublattices. The 3rd band is distinguished from the other bands by its large population at $\mathbf{k}$ = ($\pm\, 2k_{\mathrm{L}}$, $\pm\, 2k_{\mathrm{L}}$).

Figure S4 (B) shows the measured evolution of the momentum distribution of a BEC during the coherent transfer scheme. The initial state dramatically changes its distributions and the feature of

the 2nd band is well reproduced around ~ 40 μs. At each evolution time, the wave function of a BEC is well described by a certain superposition of the three eigenstates as

$$|\psi\rangle = c_1|1\mathrm{st}\rangle + c_2 e^{i\alpha}|2\mathrm{nd}\rangle + c_3 e^{i\beta}|3\mathrm{rd}\rangle, \qquad (10)$$

where the parameters c_1, c_2, c_3, α and β are chosen to be real and satisfy $\sum_{i=1}^{3} c_i^2 = 1$. Since the basis states $|1\mathrm{st}\rangle$, $|2\mathrm{nd}\rangle$, and $|3\mathrm{rd}\rangle$ are far from the eigenstates during the transfer process, these parameters show complicated time evolutions. By regarding them as free parameters, we fit the experimental data with the distribution $\left|\langle \mathbf{k}|\psi(t)\rangle\right|^2$ to obtain the band populations c_i^2 (i = 1, 2, 3). In fitting, relative intensities of the coherent peaks in the region $-4k_L \le k_x \le 4k_L$ and $-4k_L \le k_z \le 4k_L$ are used. Obtained evolutions of the band populations are plotted in **Fig. S4 (C)**, which confirms the efficient transfer into the 2nd band and show agreement with band mapping measurement in the main paper. Rather scattered data points might be due to the fitting to small coherent peaks whose intensities are largely affected by the background noise, or the systematic contribution from the higher energy bands.

S4. Effect of interactions on inter-sublattice oscillations of a BEC

In **Fig. 4 (C)** of the main paper, we compare the measured frequencies of inter-sublattice oscillations of a BEC with the relevant band gaps obtained by single particle band calculations. Systematic deviation from the prediction is found especially in the regime of small s_{diag}. We experimentally examine the effect of interactions on the oscillation frequencies by changing total atom number of a BEC, at several diagonal lattice depths shown in **Fig. S5 (A)**.

Assuming that the system is locally uniform, introduction of a local chemical potential $\mu(\mathbf{r}) = \mu - V(\mathbf{r})$ leads to the expression of the total atom number $N = \int d^3 r\, n(\mu(\mathbf{r}))$, where $V(\mathbf{r})$ is an external harmonic confinement and $n(\mu)$ is the density averaged over a unit cell. For a uniform, weakly interacting BEC, the chemical potential has a linear dependence on atomic density, leading to $N^{2/5}$ dependence of the central density $n(\mu(0))$. Therefore, we plot the observed oscillation frequency as a function of $N^{2/5}$ in **Fig. S5**. For each case, an extrapolation to the zero density seems to reproduce the expected band gap. Remaining errors of ~ 200 Hz can be accounted by uncertainty in the calibration of the lattice depths. Systematic errors in the oscillation measurements can also come from finite lifetime (~ 1 ms) of a condensate in the excited bands, which matters especially in the low frequency modes.

Whereas the negative shifts of the oscillation frequencies are observed in small s_{diag}, the shifts turn into positive around the Lieb lattice condition s_{diag} = 9.5. This tendency can be qualitatively explained by considering the density distribution of each band. For small s_{diag}, E_A becomes much lower than E_B and E_C and the wave function of the lowest band concentrates on the A-sublattice, whereas the 2nd and 3rd bands have population in both the B- and C-sublattices. The existence of a repulsive interaction shifts the energy upwards by a greater amount for the lowest band, leading to the reduction of the gaps to the higher bands. On the other hand, at s_{diag} ~ 9.5 the ground state wave function spreads over all sublattices and the amount of energy shift will decrease. The

oscillation frequencies may depend on the initial preparation, i.e., the fraction of each eigenstate. The initial conditions for the measurement in **Fig. S5** are listed in **Table S1**.

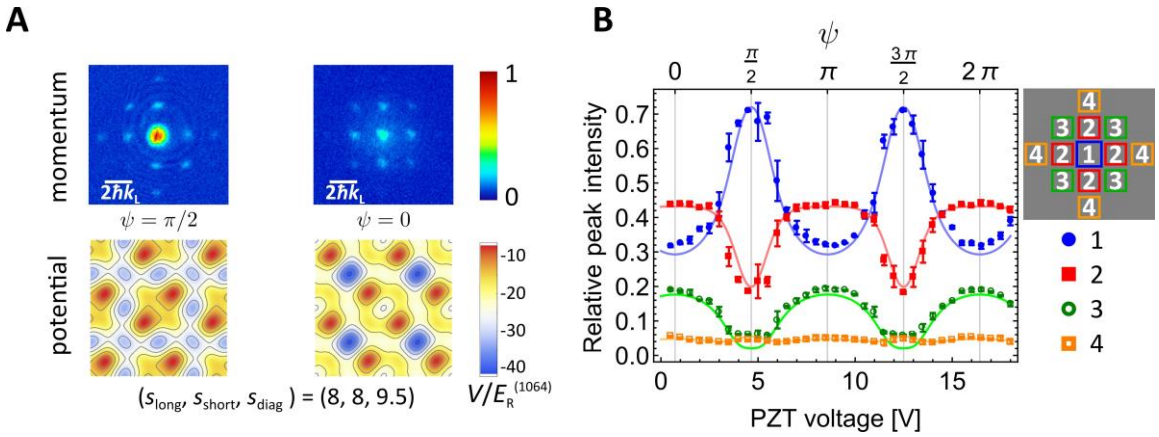

Fig. S1. Phase dependence of a time-of-flight signal.

(A), Absorption images of a ^{174}Yb BEC released from the optical lattice with $\psi = \pi/2$ (left) and $\psi = 0$ (right), taken after 14 ms of ballistic expansion. Corresponding lattice potentials are also shown.

(B), Intensities of the coherent momentum peaks of a BEC as a function of the phase ψ, measured by the time-of-flight experiment. Each peak is categorized into four, as shown in the right of the data plot. Solid lines show the result of single particle band calculation, for which horizontal offset and scale are adjusted to match the experimental data. Error bars denote standard deviation of three independent measurements.

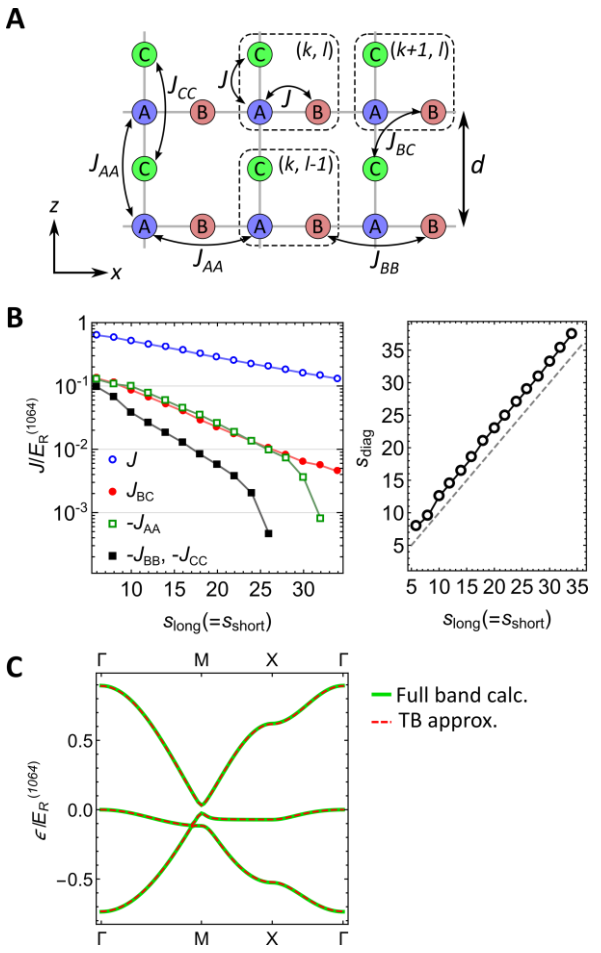

Fig. S2. Tunneling parameters in the optical Lieb lattice.

(A), Tight binding model for the Lieb lattice with beyond-nearest-neighbor hopping.

(B), (left) Tunneling amplitudes obtained from the tight-binding approximation are shown as a function of lattice depth. The solid lines are linear interpolations for the successive data points. Signs of J_{AA}, J_{BB} (J_{CC}) are inverted to display in a log scale. (right) Selected diagonal lattice depth s_{diag} to satisfy $E_A = E_B = E_C$. The dashed line represents $s_{diag} = s_{long}$ (= s_{short}) for reference.

(C), Band structure of the Lieb lattice with (s_{long}, s_{short}, s_{diag}) = (20, 20, 23). Dispersion relations of the lowest three bands of the first-principle band calculation (green solid) are well reproduced by the tight binding approximation presented here. The best fit hopping parameters are J = 0.282, J_{BC} = 0.022, J_{AA} = -0.026, J_{BB} = J_{CC} = 0.0057, E_A = 0.140 and E_B = E_C = -0.058, in unit of $E_R^{(1064)}$. The origin of the energy is set to the 2nd band at the Γ point.

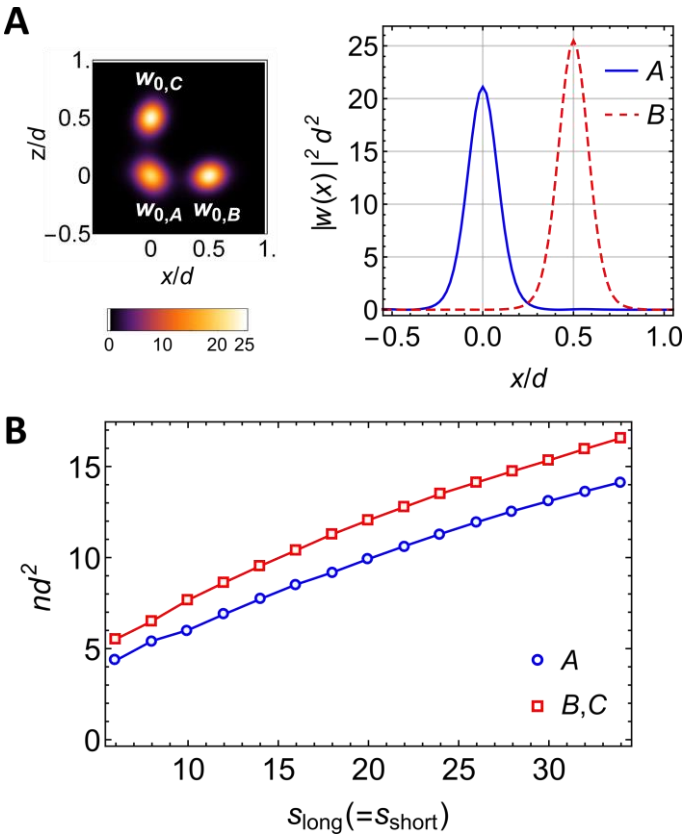

Fig. S3. Wannier functions of the optical Lieb lattice.

(A), Wannier functions of the Lieb lattice composed of the lowest three bands, at the lattice depths of (s_{long}, s_{short}, s_{diag}) = (20, 20, 23). Scaled densities $|w_{0,S}(x, z)|^2 d^2$ are shown. Density profiles of the Wannier functions on *A* and *B* sites along the $z = 0$ line are also shown in the right hand side.

(B), Average densities of the 2D Wannier functions of the Lieb lattice are plotted as a function of lattice depth. The solid lines are linear interpolations for the successive data points.

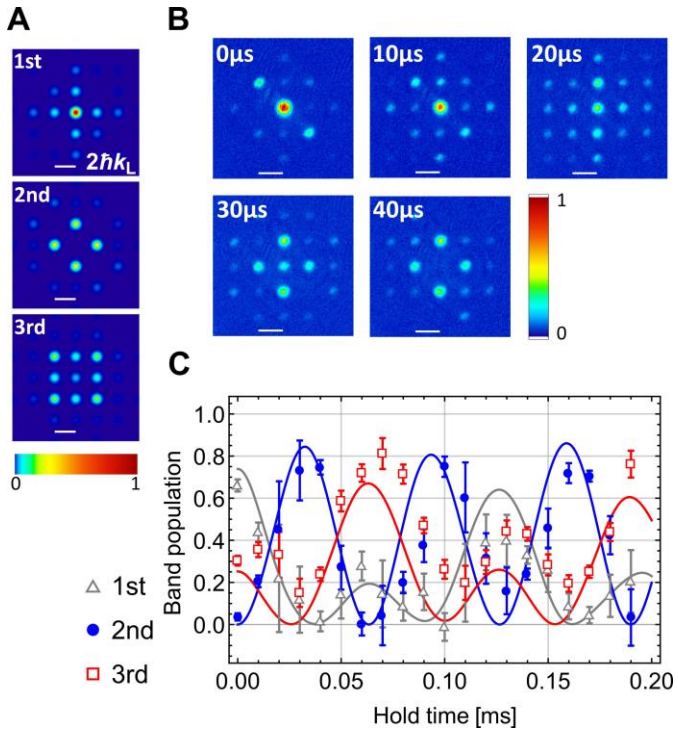

Fig. S4. Momentum space observation of coherent band transfer.

(A), Numerically calculated momentum distributions of the zero-momentum eigenstates of the lowest three bands. Potential depths are set to (s_{long}, s_{short}, s_{diag}) = (8, 8, 9.5).

(B), Evolution of the momentum distribution of a BEC during coherent band transfer. Each absorption image is taken after 14 ms of ballistic expansion.

(C), Oscillations of the band populations during coherent band transfer. Each population is obtained by fitting time-of-flight images with the momentum distribution of the superposition of the lowest three bands. Solid lines are theoretical expectation, using the parameters obtained by fitting to the band mapping measurement in **Fig. 2 (C)** of the main paper. Error bars denote standard errors in fitting procedure.

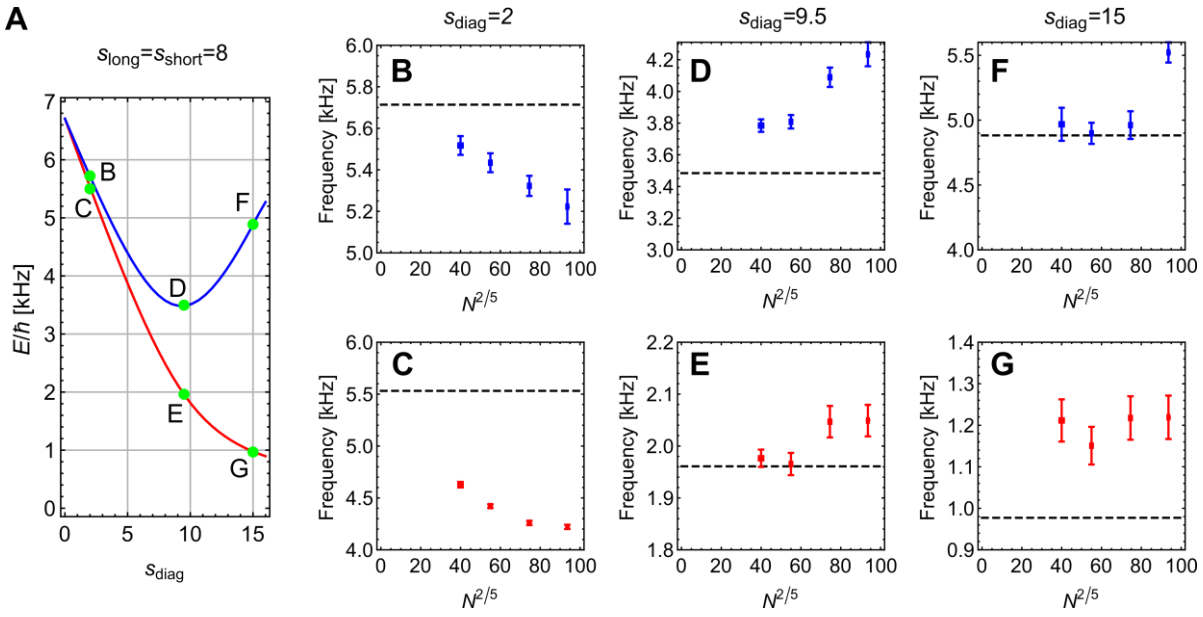

Fig. S5. Density dependence of oscillation frequency.

(A), Numerically calculated band structures of the optical Lieb lattice, as a function of s_{diag}. Green circles are the points where the measurements in **(B)-(G)** are performed, with corresponding alphabet symbols.

(B)-(G), Density dependence of inter-sublattice oscillation frequency. Horizontal dashed lines indicate the band gap from single particle calculations shown in **(A)**. Error bars denote standard errors in fitting procedure.

s_{meas} $[s_{long}, s_{short}, s_{diag}]$	s_{init} $[(s_{long}^{(x)}, s_{long}^{(z)}), (s_{short}^{(x)}, s_{short}^{(z)}), s_{diag}]$	$\lvert\langle 1, meas \rvert init\rangle\rvert^2$	$\lvert\langle 2, meas \rvert init\rangle\rvert^2$	$\lvert\langle 3, meas \rvert init\rangle\rvert^2$
1st-2nd				
(8, 8, 2)	((7.6, 0), (8.7, 29), 6)	0.964	0.033	$< 10^{-6}$
(8, 8, 9.5)	((7.5, 0), (5.9, 29), 8.4)	0.723	0.275	$< 10^{-6}$
(8, 8, 15)	((7.8, 0.03), (3.81, 29), 10)	0.571	0.426	$< 10^{-5}$
1st-3rd				
(8, 8, 2)	((8, 8), (8, 8), 20)	0.270	0	0.686
(8, 8, 9.5)	((8, 8), (8, 8), 20)	0.739	0	0.253
(8, 8, 15)	((8, 8), (8, 8), 20)	0.977	0	0.022

Table S1. Initial conditions for the inter-sublattice oscillations.

For each set of lattice depths s_{meas} at which oscillations are observed, we prepare appropriate initial state by loading a BEC into the lattice with depths s_{init}, and drive oscillations by suddenly changing the depth to s_{meas}. Calculated overlap between the initial wave function $|\mathrm{init}\rangle$ and each zero-momentum eigenstate of the measurement stage $|n,\mathrm{meas}\rangle$ (n = 1, 2, 3) is also shown.